

Accepted manuscript doi: 10.1680/jgeot.19.P.277

Accepted manuscript

As a service to our authors and readers, we are putting peer-reviewed accepted manuscripts (AM) online, in the Ahead of Print section of each journal web page, shortly after acceptance.

Disclaimer

The AM is yet to be copyedited and formatted in journal house style but can still be read and referenced by quoting its unique reference number, the digital object identifier (DOI). Once the AM has been typeset, an ‘uncorrected proof’ PDF will replace the ‘accepted manuscript’ PDF. These formatted articles may still be corrected by the authors. During the Production process, errors may be discovered which could affect the content, and all legal disclaimers that apply to the journal relate to these versions also.

Version of record

The final edited article will be published in PDF and HTML and will contain all author corrections and is considered the version of record. Authors wishing to reference an article published Ahead of Print should quote its DOI. When an issue becomes available, queuing Ahead of Print articles will move to that issue’s Table of Contents. When the article is published in a journal issue, the full reference should be cited in addition to the DOI.

Submitted: 23 September 2019

Published online in ‘accepted manuscript’ format: 25 June 2020

Manuscript title: Numerical modelling of a structure with shallow strip foundation during earthquake-induced liquefaction

Authors: Konstantinos Kassas*, Orestis Adamidis*, Nikos Gerolymos[†] and Ioannis Anastasopoulos*

Affiliations: *ETH Zurich, Switzerland and [†]NTUA, Greece

Corresponding author: Ioannis Anastasopoulos, ETH Zurich, Switzerland.

E-mail: ioannis.anastasopoulos@igt.baug.ethz.ch

Abstract

Structures with shallow foundations are susceptible to excessive settlement and rotation in the event of earthquake-induced soil liquefaction. Numerical modelling of the problem remains challenging, due to persisting uncertainties regarding dynamic soil response and soil-structure interaction. This paper employs numerical simulations to study the seismic response of a structure on a shallow mat foundation, resting on a liquefiable sand layer. A coupled hydromechanical analysis is performed employing the finite differences code FLAC2D, modelling nonlinear soil response with the constitutive model PM4Sand. A broad set of element tests on Hostun sand (widely used in centrifuge modelling) are performed and used for extensive model calibration. The calibrated model is then validated against centrifuge test results. The validation is not restricted to the recorded pore pressure, acceleration, and settlement time histories, but extends to the deformation mechanisms extracted from centrifuge test through image analysis, allowing for an in-depth assessment of the numerical simulation. Overall, the analysis is in good agreement with the centrifuge model test. The pore pressure build-up and the final foundation settlement and displacement fields are predicted with adequate accuracy. Although the accumulated displacements are well reproduced, the failure mechanism is not fully captured. This discrepancy is attributed to dissipation – related phenomena, which are not accurately reproduced in the numerical analysis.

Keywords: centrifuge modelling; earthquakes; footings/foundations; laboratory tests; liquefaction; numerical modelling

1. Introduction

Buildings with shallow foundations resting on liquefiable layers can experience significant settlement, tilt and even suffer complete bearing capacity failure. Although such structures are the most common, they are not sufficiently protected, as showcased during recent events in New Zealand (Cubrinovski et al. 2011), Japan (Yasuda et al. 2013) and Indonesia (Sassa and Takagawa 2019).

The state of practice for the prediction of liquefaction-induced settlement of a structure typically employs free-field methods. Such methods focus on consolidation in the free-field, ignoring shear strains in the vicinity of the foundation (due to the dead load of the superstructure) and soil-structure-interaction (Dashti et al., 2010). Nevertheless, experimental evidence from centrifuge model tests has shown that the settlement of structures on shallow foundations is primarily due to shear strains, while sedimentation and consolidation are of minor significance (Adamidis and Madabhushi, 2018). Moreover, they reveal that the developing deformation mechanism is a function of the depth of the soil that liquefies and of the bearing pressure applied by the foundation, both of which strongly affect the final accumulated settlement (Adamidis and Madabhushi 2018).

Despite the valuable insights gained from such centrifuge experiments, a comprehensive study of the problem through centrifuge modelling is extremely resource-demanding due to the large number of parameters that need to be investigated. A more viable option is the use of numerical nonlinear deformation analyses (NDAs), employing advanced constitutive models that can capture the nonlinear stress-strain response of liquefiable soil. Such models require a large set of element test data for calibration. Before conducting parametric studies, careful validation against experimental results of boundary value

problems is necessary (e.g., Bullock et al. 2018; Bray and Macedo, 2017; Tasiopoulou & Chaloulos, 2019).

This paper employs numerical simulations to study the seismic response of a structure on a shallow mat foundation, resting on a shallow layer of liquefiable sand. The analysis is performed employing the advanced constitutive model PM4Sand (Boulanger and Ziotopoulou 2017), as implemented in the finite difference (FD) code FLAC (Itasca 2016). An extensive set of element tests on Hostun sand were performed at the ETH Zurich geotechnical laboratory, and are used for thorough calibration of the constitutive model. This is a first key contribution of the paper, as Hostun sand is widely used in centrifuge model tests (e.g., Okay et al., 2014; Adamidis and Madabhushi, 2016) and the experimental dataset will be useful to the research community for future model calibration and validation. The calibrated model is then validated using one of the centrifuge experiments of Adamidis & Madabhushi (2018) as a benchmark. In addition to accelerations, pore pressures, and foundation-structure response (settlement and rotation), the validation extends to the developing deformation mechanisms, which were captured in the centrifuge test through image analysis (Adamidis & Madabhushi 2018). This is a second key contribution of the paper, which allows an in-depth assessment of the numerical simulation, revealing strengths and limitations, but also the potential reasons of the observed discrepancies.

2. Laboratory testing of Hostun sand

A comprehensive series of element tests were conducted at the ETH Zurich geotechnical laboratory to fully characterize Hostun HN31 sand. The scope of the conducted tests goes beyond the needs of the specific study, aiming to offer a reference dataset for future model calibrations and validations.

Widely used in centrifuge modelling in the University of Cambridge, but also in the French institute of science and technology for transport, development and networks (IFSTTAR), Hostun HN31 sand is a fine sub-angular to angular siliceous sand (Adamidis et al., 2020). It has a mean particle diameter $D_{50} = 0.341$ mm and soil particle density $G_s = 2.65$. The coefficient of uniformity is $C_u = 1.47$ and the coefficient of curvature is $C_c = 0.98$. The limiting void ratios were measured to be $e_{min} = 0.671$ and $e_{max} = 1.049$, according to ASTM D4253-00 (2006) and ASTM D4254-00 (2006). Regarding the minimum void ratio it was found that a denser state could be achieved by air pluviation ($e_{min} = 0.648$). Therefore, this value was adopted as the minimum void ratio in this study. The limiting void ratios determined in this study differ only slightly from those reported by Flavigny et al. (1990) and Fargeix (1986).

Three different types of tests were conducted and are discussed in detail in the next sections: (a) triaxial tests with embedded bender elements, to measure small-strain shear modulus; (b) Cyclic direct simple shear (DSS) tests, to measure shear modulus degradation and damping ratio; and (c) constant volume direct simple shear tests (CVDSS), to determine cyclic stress resistance.

Small-strain shear modulus

The small-strain shear modulus (G_{max}) is estimated using bender elements embedded in the triaxial testing devices of the ETH Zurich Institute for Geotechnical Engineering (IGT), obtaining measurements for triaxial specimens of different relative densities at different stress levels. The triaxial devices were initially designed for tests on snow (Bartelt and von Moos 2000) and were later modified for soil testing (Arenson & Springman 2005). A detailed description is offered in Trausch-Giudici (2004).

Bender elements were introduced by Shirley (1978); Shirley & Hampton (1978) for measuring the small-strain shear modulus (G_{max}) of soil specimens. A pair of bender elements are typically embedded in a soil specimen, the first acting as a transmitter and the second as a receiver. Through bending, the transmitter generates a shear excitation of controllable frequency, generating shear waves that travel through the soil specimen, reaching the receiver and subjecting it to bending. By comparing the transmitted to the received signal, the travel times of the generated shear waves are used to calculate the small-strain shear wave velocity V_s , and thus the small-strain shear modulus G_{max} of the specimen.

The specimens were prepared in a specially fabricated mould by wet pluviation of Hostun sand in de-aired water. The sand was densified to the required relative density by tapping. The triaxial specimens (**Fig. 1a**) had a diameter of approximately 55 mm and a height of approximately 130 mm. B value tests (Skempton, 1954) yielded values above 98% for all specimens. The required level of mean effective stress before each bender element measurement was obtained by isotropic consolidation. The utilized bender elements were installed on the top and bottom cap of the triaxial device by the Enel-Hydro company (Bergamo, Italy), protruding into the specimen by 1.6 mm. The experimental setup is depicted in **Fig. 1b**. A 100 MHz Synthesized Arbitrary Waveform Signal Generator by Wavetek (model 395) was used to generate the signals, and a WaveSurfer 424 oscilloscope (200MHz) by LeCroy was used to capture the data.

Single-shot sinusoidal pulses were used as excitation, as they reduce frequency components (Blewett et al. 2000) and allow identification of points of similarity between input and output. Nevertheless, even with single frequency sinusoidal pulses, multiple frequency components still exist at the output (Blewett et al., 2000). For the determination of travel time, a multitude of methodologies have been proposed, with a consensus not yet

having been reached. In this study, after thorough comparative assessment of various options proposed in the literature (Arulnathan et al., 1998; Viggiani and Atkinson, 1995; Lee and Santamarina, 2005) the point of first arrival was used to determine travel time, as it was found to lead to the most reliable results. This method takes the travel time as the time difference between the beginning of the input pulse and the first arrival of the wave at the output trace. It assumes plane wave fronts and absence of reflected or refracted waves (Arulnathan et al., 1998).

Selecting the point that corresponds to first arrival can be challenging (Arulnathan et al., 1998; Lee and Santamarina, 2005). As shown in **Fig. 2**, points *A*, *B*, *C* or *D* could be taken as corresponding to first arrival. Lee & Santamarina (2005) proposed a more complex signal-matching technique for calculating V_s and concluded that if point *C* (“zero after first bump”) is taken as the first arrival, the difference between the shear wave velocities calculated with the two methods is a mere 1%. In the results presented herein, first arrival was calculated using the “zero after first bump”. The travel length was taken as the tip-to-tip distance between transmitter and receiver bender elements (Dyvik & Madshus, 1985).

Specimens were prepared at three void ratios: $e = 0.879, 0.852$ and 0.822 corresponding to relative densities $D_r = 42, 49$ and 57% , respectively. Measurements were taken at five mean effective stress levels: 5, 20, 100, 200, and 400 kPa. For each combination of void ratio and effective stress, 19 single-shot sinusoidal pulses were used as shear wave excitations, with frequencies starting at 2 kHz and increasing by 1 kHz up to 20 kHz. An average of the travel time estimated for each pulse was used to calculate the shear wave velocity. The produced curves of G_0 versus mean effective stress are presented in **Fig. 3**, where the initial void ratios of the specimens are quoted, even though for the calculation of V_s and G_0 the changes in height and void ratio with increasing p' were accounted for.

The calculated small-strain shear modulus G_0 was compared with the published analytical expression of Azeiteiro et al. (2017). Their results are based on a series of bender element measurements, which were performed on air-pluviated triaxial samples of Hostun sand. The comparison between the obtained results (this study) and the analytical expression of Azeiteiro et al. (2017) is presented in **Fig. 4**. For a better visual comparison,

$G_{max}/(p_a \left(\frac{p'}{p_a}\right)^m)$ is plotted versus the void ratio, with both G_{max} and p_a expressed in kPa.

The expression proposed by Azeiteiro et al. (2017) fits well to the values calculated:

$$G_{max}(kPa) = 29300 \frac{(2.97 - e)^2}{1 + e} \left[\frac{p'}{100} \right]^{0.49} \quad (1)$$

Shear Modulus degradation and damping ratio

Cyclic direct simple shear (DSS) tests were performed on the NGI direct simple shear apparatus of IGT to assess the degradation of shear modulus (G) and the increase of damping ratio (ξ) with shear strain and initial vertical effective stress (σ'_{vo}). The NGI device was designed by the Norwegian Geotechnical Institute and manufactured by Geonor (1968). The initial design was later modified to allow stress- or strain-controlled shearing and controlled vertical loading. An electric screw jack actuator was added to control vertical loading, combined with a 4 kN capacity load cell. Another electric screw jack actuator was added to apply horizontal shearing to the specimen, while linear variable differential transformers (LVDTs) record both vertical and horizontal displacements. Finally, a new control system was implemented, allowing control of stress and strain loading. The modified apparatus is presented in **Fig. 5a**.

The DSS apparatus allows uniform shearing of a soil specimen throughout its volume. The top plate translates horizontally relative to the fixed base, while the specimen is confined in a wire reinforced rubber membrane (**Fig. 5b**), which does not allow the development of

radial strain during the test, forcing the horizontal cross sectional area of the specimen to remain constant. The membranes used were reinforced with iron-nickel wire of 0.15 mm diameter, wound around the membrane 27 times per cm of height.

The sand specimens were prepared in the wire reinforced rubber membrane by dry pluviation and were then tapped to reach the target relative density. All specimens had a cross sectional area of 50 cm² and a height which varied between 21 mm and 24 mm. After preparation, each specimen was installed in the DSS apparatus and loaded to the target vertical stress. When the target vertical stress was reached, it was maintained constant until the rate of settlement fell below 1 µm/10 min, and only then was the specimen subjected to shearing.

The shear modulus and damping ratio evolution with shear strain were determined for 3 different vertical stresses (50, 100, and 150 kPa) and three different void ratios. The results from a typical experiment with void ratio $e = 0.829$ at initial vertical effective stress $\sigma'_{vo} = 50$ kPa are presented in **Fig. 5c,d** in terms of shear stress–shear strain ($\tau - \gamma$) and volumetric strain–shear strain ($\varepsilon_v - \gamma$) response. The sample was sheared at 3 different levels of shear strain, applying 20 load cycles at each strain level. The shear modulus for each strain level was determined from the inclination of the maxima and minima of stress – strain loops (**Fig. 6a**); the damping ratio is calculated according to Eq. (2), where ΔW is the dissipated energy at each load cycle and W is the maximum elastic energy stored for each cycle.

$$\xi = \frac{1}{4\pi} \frac{\Delta W}{W} \quad (2)$$

In **Fig. 6a,b**, the measured shear modulus degradation and damping ratio are compared with the analytical expression of Ishibashi and Zhang, (1993), produced on the basis of the small-strain stiffness measured from the bender element tests, and assuming K_0 conditions during shearing. K_0 was calculated through the critical state friction angle ϕ_{cv} , as presented in

Table 3. A good fit is observed between the analytical expression and the measured values for all three tests, which implies that the analytical expression of Ishibashi & Zhang (1993) offers a good approximation for Hostun (HN31) sand, while giving confidence in the values of small-strain shear modulus determined from bender element measurements. Moreover, through this procedure we can obtain information for the region ($\gamma < 0.1\%$), where measurements could not be made accurately with the used DSS apparatus.

Cyclic stress resistance

For the determination of the liquefaction potential of Hostun HN31 sand, an extensive series of constant volume direct simple shear tests were performed (CVDSS). Constant volume tests were introduced by Taylor (1948) for triaxial conditions; Pickering (1969) applied the concept to cyclic simple shear tests of soil specimens constrained within rigid walls. The volume of the specimen is maintained constant during shearing by locking the vertical actuator to zero displacement. Cyclic shearing of loose samples leads to a tendency for contraction, which translates to a progressive reduction of vertical stress. This drop of vertical stress is equal to the increase in pore water pressure of a corresponding undrained test (Finn and Vaid 1977). Following this procedure, the liquefaction susceptibility of a fully saturated sand can be determined using dry specimens, thus increasing efficiency. Dyvik et al. (1987) showed that the drop in the vertical stress during shearing of constant volume direct shear tests is equal to the excess pore pressure developed during undrained tests. Finn & Vaid 1977 conducted several such experiments and concluded that there is no practical difference between experiments with dry and saturated sand specimens.

Overall, 12 CVDSS tests were conducted, prepared as described previously for DSS tests. An initial vertical stress $\sigma'_{vo} = 100 \text{ kPa}$ was applied. **Fig. 7 (left side)** presents typical CVDSS results for a specimen of initial void ratio $e = 0.836$ at initial effective vertical stress of 100 kPa. The sample was sheared at a cyclic stress ratio $CSR = \tau/\sigma'_{vo} = 0.119$ and

liquefaction triggering was observed after the 15th load cycle. Triggering of liquefaction is assumed to be at the point where the shear strain becomes equal to 3.75% in single amplitude (SA). Interestingly, this criterion was found to coincide with the point at which the excess pore water pressure ratio $r_u = \Delta u / \sigma'_{vo}$ reached 98 %. Soils do not necessarily reach the strain threshold for liquefaction with a full excess pore water pressure and liquefaction particularly in dense sands may be triggered with r_u even below 0.8 (Wu et al., 2004). Indeed, here it is observed that the largest discrepancies between the two criteria are observed for the case of the denser samples ($e = 0.717$).

Fig. 8 shows the cyclic resistance curves obtained for Hostun (HN31) sand for initial vertical effective stress $\sigma'_{vo} = 100 \text{ kPa}$. Each curve depicts the number of cycles required to trigger liquefaction in function of cyclic stress ratio and void ratio. As summarized in **Table 1**, three different void ratios were examined: $e = 0.915, 0.832$ and 0.717 corresponding to relative densities $D_r = 33, 54$ and 83% , respectively. For each void ratio, four cyclic stress ratios were examined. In all cases examined, the two liquefaction triggering criteria were found to coincide in terms of load cycles (N) for liquefaction triggering. An analytical exponential expression (Eq. 3) is fitted to the results, offering a prediction of the cyclic stress resistance (CRR) as a function of void ratio e and number of cycles to liquefaction N .

$$CRR = (-1.078e + 1.114)N^{(0.179e - 0.330)} \quad (3)$$

The curves given by Eq. 3 (dotted lines in the figure) are compared to the experimental measurements (points), demonstrating the effectiveness of the fit. Moreover, Eq. 3 demonstrates the dependency of the slope of the power relationship on density.

6. Calibration of constitutive model

The seismic response of fully saturated Hostun (HN31) sand is simulated using the plane-strain, stress-ratio controlled, critical state compatible, bounding surface plasticity model PM4Sand, Version 3.1 (Boulanger and Ziotopoulou 2017). The model has been developed for geotechnical earthquake engineering applications, following the framework of the DM04 model (Dafalias and Manzari 2004). PM4sand has been shown to be capable of predicting soil behaviour under cyclic loading at different relative densities, under different confining pressures and stress paths. A detailed description of model formulation and its modifications can be found in Boulanger and Ziotopoulou (2013), Ziotopoulou & Boulanger (2016) and Boulanger and Ziotopoulou (2017).

Accurate modelling of cyclic soil response is the key for successful simulation of centrifuge model tests. PM4Sand comprises 27 input parameters, from which 6 are considered primary (including the atmospheric pressure and 2 “flag” parameters) and 21 secondary. The primary parameters include the apparent relative density (D_r), the small-strain shear modulus coefficient (G_o) and the contraction rate parameter (h_{po}). Preset values, which are generally functions of an index property, can be used for the secondary parameters, or they can be calibrated against experimental data. To that end, the previously discussed soil element test results were used for an extensive calibration of the parameters of the constitutive model.

Table 2,3 summarize the calibrated analysis parameters for Hostun (HN31) sand and PM4sand, considering the relative density of the centrifuge model test that is to be numerically simulated. The limiting void ratios e_{min} and e_{max} were measured at the ETH Zurich geotechnical laboratory (as previously discussed). The relative density (D_r),

porosity (n), wet and dry densities (ρ_s , ρ_s) were calculated directly from the void ratio of the centrifuge model test. The critical state friction angle ϕ_{cv} was measured from the previously discussed drained triaxial tests (conducted in ETH Zurich) and used to calculate the lateral earth pressure coefficient at rest K_0 and the Poisson's ratio ν , as shown in **Table 3**. Bolton (1986) constants for the description of critical state were estimated to be $Q = 8.4$ and $R = 0.78$ using triaxial test results.

The small-strain shear modulus coefficient G_o was calculated for the desired void ratio using the analytical expression of Azeiteiro (2017), validated in the present study against bender element tests (**Fig. 4**). The permeability (k) was calculated using the analytical expression of Kozeny-Carman (Eq. 4), which was shown by Adamidis et al. (2020) to offer good results for Hostun (HN31) sand:

$$k = \frac{\rho_w g}{\eta} \times \frac{1}{C_{CK}} \times \frac{1}{S^2} \times \frac{e^3}{1+e} \quad (4)$$

The empirical constant C_{CK} was given its typical value of 5 (Carrier 2003), while the ratio of surface to volume of soil particles (S) was estimated according to the morphology analysis of Adamidis et al. (2020). The last parameter calibrated is the contraction rate parameter (h_{po}), which was set by targeting the relevant cyclic stress resistance curve for Hostun (HN31) sand, calculated using Eq. 3 (**Fig. 8**).

Fig. 7 compares the FLAC numerical prediction (using the calibrated PM4sand) to direct simple shear test results in terms of: (a) shear stiffness degradation; (b) stress path; and (c) vertical effective stress degradation with load cycles. The shear stress–shear strain response and the stress path evolution are predicted reasonably well. However, two important points need to be made. Firstly, the model cannot simulate the abrupt drop of effective vertical stress during the first load cycle (**Fig. 7b,c**), predicting a steeper decrease

of initial vertical stress prior to liquefaction triggering (after 10 loading cycles). Secondly, the two liquefaction triggering criteria do not coincide in the analysis, as was the case for the specific experimental results. More specifically, for $e = 0.836$, $\sigma'_{vo} = 100 \text{ kPa}$ and $CSR = 0.119$, the numerical model predicts 17 load cycles to reach the 3.75% shear-strain criterion, while only 12 load cycles are required according to the pore pressure built-up ($r_u = 98 \%$) criterion (**Fig. 7c**). This can be crucial for the simulation of a boundary value problem, as the result will largely depend on the chosen liquefaction-triggering criterion. Moreover, the inability of the constitutive model to capture the abrupt effective stress drop of the first load cycle may have implications on the prediction of the initial settlement rate of a structure during seismic shaking.

Fig. 9a presents indicative results of (single-element) cyclic undrained strain-controlled simple shear numerical analysis, calibrated for the density of the centrifuge test. The numerical prediction is compared to the experimental (element testing) results in terms of number of uniform cycles required to reach the two criteria (3.75% shear strain and $r_u = 98 \%$) against the CSR . As previously mentioned, in the numerical analysis there is a discrepancy between the two liquefaction-triggering criteria (pore pressure build-up and accumulated shear strains). For example, for $CSR = 0.2$ the model predicts liquefaction after 4 load cycles based on the pore pressure build-up criterion, but 4 more cycles are needed for the accumulated shear strain to reach the 3.75% SA shear-strain threshold. This implies that a selection of the liquefaction-triggering criterion is necessary, depending on the studied problem and the key behaviour that has to primarily be captured. In this study, the average of the cycles calculated by each of the two criteria is used for model calibration.

A second issue regarding the calibration of h_{po} is illustrated in **Fig. 9b**, where it is shown that it was not possible to capture the targeted *CRR* curve over a wide range of *CRR* values. To tackle this issue, a range of interest of 0 to 20 load cycles was selected, which is considered sensible for earthquake-related problems. To reduce the discrepancy between the experimental and the numerical curves within the range of interest, $h_{po} = 0.04$ was selected. The discrepancy between the two liquefaction-triggering criteria can be minimized by reducing the small-strain (initial) shear modulus G_o . As shown in **Fig. 9c,d**, by reducing the initial shear modulus to $0.6G_o$, the *CRR* curve according to the pore pressure build-up ($r_u = 0.98$) criterion is only marginally affected (**Fig. 9c**), while the one corresponding to the 3.75% accumulated shear strain criterion moves to the left (**Fig. 9d**). However, using such reduced small-strain shear modulus is not consistent with the element test results, and was therefore not pursued further.

7. Modelling of Centrifuge Test

The calibrated constitutive model is employed to simulate numerically a centrifuge experiment that modelled the seismic response of a plane strain structure with a shallow strip foundation resting on a shallow layer of saturated sand. By comparing the numerical prediction to the centrifuge test results, the efficiency of the constitutive model can be assessed, offering insights on the sensitivity of the numerical analysis results to key model parameters, and setting the base for future parametric analyses. Moreover, the combined numerical and experimental simulation offers deeper understanding of the mechanisms leading to foundation settlements.

Experimental setup

The centrifuge model test (OA6) was conducted on the Turner Beam Centrifuge of the Schofield Centre at the University of Cambridge (Adamidis and Madabhushi 2018). As shown in the cross-section of **Fig. 10** a rigid superstructure on a foundation of width $B = 4.62$ m (in prototype scale) was tested, having an aspect ratio $\frac{h_{cm}}{B} = 0.58$ (with h_{cm} being the height of the centre of mass, measured from the foundation base). The soil stratum was a shallow Hostun (HN31) sand layer of void ratio $e = 0.788$, and depth equal to the foundation width B . The model was prepared by air pluviation in a rigid container equipped with a Perspex window and tested at 50 g. The fluid viscosity was scaled using a de-aired aqueous hydroxypropyl methylcellulose solution, prepared according to Adamidis & Madabhushi (2015) to be 50 times more viscous than water, in order to render compatible dynamic and pressure dissipation time scaling.

Images captured through the Perspex window using a high frame rate camera were used for Particle Image Velocimetry analysis (White et al., 2003), from which displacement fields were produced. Nevertheless, the use of a rigid container inevitably introduced boundary effects, which were alleviated using a material called Duxseal (Parker Hannifin Corporation, 2013) at the lateral model boundaries. Its effectiveness has been examined by Steedman & Madabhushi (1991), who concluded that it is able to absorb about 65% of incident wave energy for P and S waves. As illustrated in **Fig. 10**, the instrumentation included miniature pore pressure transducers (PPT), piezoelectric accelerometers (Acc), microelectromechanical system accelerometers (MEMS) and linear variable displacement transducers (LVDT). More details can be found in Adamidis and Madabhushi, (2018)

Numerical Modelling

The numerical simulations are performed using the FD code FLAC 8.0 (Itasca 2016). A nonlinear, coupled hydromechanical, effective stress, time history analysis is conducted, incorporating the PM4sand (Version 3.1) constitutive model, thoroughly calibrated against the conducted element tests, as previously discussed.

Fig. 11 shows the finite difference mesh, model geometry, interface and water table location. The Duxseal is modelled as linear elastic, with its permeability set 100 times lower than the permeability of the adjacent soil. Analysing one-dimensional compression test results, Popescu & Prevost (1993) concluded that the Young's Modulus of Duxseal is $E = 800 \text{ kPa}$, its Poisson's ratio $\nu = 0.46$, and its mass density $\rho = 1.65 \text{ Mg/m}^3$. The boundary conditions imposed by the rigid container are accounted for by applying the seismic excitation at the bottom and edge nodes of the FD model, using a velocity time history corresponding to the acceleration trace that was measured at the base of the centrifuge box during testing. The bottom nodes are fixed in the vertical direction, while the side nodes are allowed to move freely in the vertical direction, simulating a zero-friction condition between the box and the Duxseal.

The structure is modelled using linear elastic beam elements of very large stiffness to model rigid body response. In the centrifuge experiment, the fixed-base frequency of the structure was selected to be higher than the frequency of the input motion, promoting a rigid-body type of response. Indeed, the measured flexural response of the structure was found to be negligible in the experiment (Adamidis & Madabhushi, 2018), justifying the assumption of a very large stiffness in the numerical analysis conducted herein. The mass density of the structural elements is set accordingly to match the bearing pressure of the

experiment (50 kPa). The width and height of the block modelling the structure are 4.62 m and 5.36 m, respectively, matching the centrifuge model test. The beam acts as an impermeable barrier and ensures that there is no upward flow below the structure. The soil-foundation interface is modelled with a frictional interface, allowing for sliding and detachment. The foundation width is discretized using 20 elements, while the friction angle at the interface is set to $\delta = 28.8^\circ$ according to measurements using a direct shear apparatus.

At the static phase prior to shaking, the Mohr Coulomb model is assigned to the soil and the elastic shear and bulk modulus of soil are calculated as a function of the void ratio and the confining stress. Afterwards, the PM4sand model is assigned to the soil elements and the mechanical (static) analysis is repeated. This is followed by a coupled hydromechanical calculation, assuming fluid bulk modulus $K_w = 2 \cdot 10^9$ kPa. Finally, the dynamic coupled hydromechanical time history analysis is performed. Following the recommendations of Boulanger & Ziotopoulou (2017), Rayleigh damping is set to 0.5 % at a center frequency of 1 Hz, which is the dominant frequency of the input motion. The PostShake Flag parameter of PM4sand is enabled after strong shaking (20 s) to improve the modeling of post-liquefaction reconsolidation strains. When this parameter is enabled, the initial shear and bulk modulus is reduced by a factor accounting for the soil's loading history through a cumulative fabric term. This is a phenomenological procedure, which has been found to provide improved modelling of post-liquefaction reconsolidation strains (Ziotopoulou (2016)). Large deformations and second order effects were taken into account by automatically updating mesh node coordinates after each analysis step.

Comparison of numerical simulation to centrifuge test

The numerical prediction is compared to the centrifuge test results in terms of accelerations, pore pressures, settlement and rotation of the structure, as well as the deformation mechanisms developed within the liquefiable layer. The prediction classifies as C1 because it was performed after the centrifuge tests with their results known (Lambe 1973). However, the analysis was based solely on the conducted element tests and no iterative adjustment was took place based on the system-level results.

In **Fig. 12**, pore pressures recorded in the centrifuge test in the free field (P2, P7 and P13) and below the structure (P1 and P10) are compared with the numerical prediction. The magnitude of excess pore pressure is well predicted in all positions in the free field (**Fig. 12a**). In all cases examined, the numerical simulation required a few additional cycles to reach the same level of excess pore pressure as that recorded in the centrifuge test. This can be attributed to the few extra load cycles required for pore pressure build-up in the numerical simulation in comparison to a CVDSS test, as was shown in **Fig. 11a**. Furthermore, the reduced excess pore pressure generation during the first load cycle also contributes to the inability of the numerical model to capture the abrupt pore pressure build-up that is observed at the beginning of shaking in the centrifuge experiment. After the end of seismic shaking (at about 20 s), dissipation of excess pore water pressures can be observed in the experiment, and is also captured by the numerical analysis.

The discrepancies between the numerical prediction and the centrifuge model test are more substantial in the area below the footing (**Fig. 12b**). During the first 5 s, the numerical model predicts suction below the footing (P10) instead of the experimentally recorded pore pressure build-up. At the base of the soil layer (P1), the numerically predicted pore pressure

build-up is significantly slower than the one recorded in the centrifuge experiment. The initial suction under the footing (P10), is attributed to the increased dilation predicted by the numerical model and the complicated fluid flow within the soil just below the foundation. At the base of the soil layer (P1), dissipation of pore pressures is initiated very early in the experiment, just after the first 2 seconds of seismic shaking. In stark contrast, in the numerical analysis it is initiated only after the end of strong shaking (at $t \approx 18 - 19$ s). As will be shown later on, such dissipation– and gradient flow–related phenomena play a significant role also during shaking.

Fig. 13 compares the numerically predicted acceleration time histories to those recorded in the centrifuge model test. In the free-field (A3, A4), the prediction is better at depth (accelerometer A3). Close to the ground surface (A4), the numerical prediction significantly overestimates the acceleration, despite the fact that the computed excess pore water pressure at the same depth (P13) compared well with the experimentally recorded (**Fig. 12**). The same issue has been observed by Finn (1988), Green (2003), and Ziotopoulou (2018), who suggested that FLAC produces high frequency “noise” in cases of saturated sands at the level of the ground surface, where the initial effective stress is particularly low (Ziotopoulou, 2018). Indeed, the acceleration under the footing (M13), where the developing excess pore water pressure is lower and thus the effective stress is higher, is adequately predicted. The comparison is equally successful for all other locations in the array below the structure, not presented herein due to space limitations. The acceleration transmitted to the structure (CM) is also over-predicted, especially during the first half of the seismic excitation.

Despite the limitations pointed out so far, the numerical prediction is successful in terms of accumulated foundation settlement (**Fig. 14**). However, the amplitude of rotation during shaking is significantly over-predicted, something that can be attributed to the over-prediction of the acceleration at the center of mass (CM) of the structure. Moreover, the settlement during the first loading cycle is significantly under-predicted. This can be attributed to the previously mentioned suction that develops below the foundation during the first 5 cycles (**Fig. 12a**). This is due to the inability of the constitutive model to capture the abrupt drop in initial effective stress during the first loading cycle (**Fig. 7b**), and differences in the developing failure mechanism, as will be discussed later on.

The observed discrepancies in the settlement–rotation response can be understood better by examining the deformation mechanisms within the liquefiable layer. In **Fig. 15**, the computed shear strain contours at the end of shaking are compared to those of the centrifuge model test, calculated using image analysis (Adamidis & Madabhushi, 2018). The numerical simulation predicts mobilization of a bearing capacity failure mechanism mainly directly below the edges of the foundation, while in the centrifuge experiment, shear strains were concentrated below the edges of the foundation and to the adjacent soil further away. In the experiment, the soil directly below the foundation (in particular towards the edges) experienced significant shearing. In the simulation, the level of accumulated shear strains under the foundation was lower. While in the experiment the primary deformation mechanism involved the displacement of soil under the edges of the foundation, in the numerical simulation the bulb of soil under the footing rotated along with the structure, displacing the surrounding soil.

The pore pressures at P1 and P10 below the footing (**Fig. 12a**), may offer an insight for these differences. Initially, the predicted suction in the area directly below the footing (P10) leads to the development of a stiff soil bulb, which can move and rotate (as a quasi-rigid body) together with the footing, without undergoing significant softening. The increased predicted pore water pressure build-up at depth (P1) leads to softening of the soil, allowing for higher levels of shearing to develop deep below the footing. In the centrifuge experiment the level of shear deformation at the soil column below the surface footing was lower.

These differences in accumulated shear strain justify the differences in the ultimate horizontal displacement contours of **Fig. 16**. While the displacement field is on average accurately predicted, both in terms of displacement amplitude and geometry, the shape of the maximum horizontal displacement contours below the edges of the foundation is different compared to that of the centrifuge experiment. This difference is consistent with the discrepancy in failure mechanisms illustrated in **Fig. 15**. Nevertheless, the numerical simulation does seem to adequately predict the displacement field of the centrifuge experiment beyond the point where it was not recorded due to space limitations in the experimental set-up.

Another potentially important limitation of the numerical simulation is the inability of the constitutive model to accurately predict plastic volumetric strains inherent to a constitutive formulation that is stress-ratio controlled and has no cap on the elastic yield surface (Ziotopoulou and Boulanger 2013b). **Fig. 17** compares the predicted ultimate vertical displacement contours to those captured in the centrifuge experiment. The simulation predicts very small volumetric strains, resulting in significant heaving at the

ground surface away from the foundation, to counteract the settlement of the structure.

This is not in agreement with the centrifuge experiment, where limited heaving was observed, only directly next to the foundation. Further away from the structure, the soil settled. Despite this shortcoming regarding volumetric strains, the settlement of the foundation is predicted reasonably well, a testament to the primarily shear nature of settlement-generating mechanisms. The dominance of a shear mechanism under the foundation, which was not observed in the experiment (as discussed above), is reflected in the deeper bulb of vertical displacements predicted by the numerical simulation.

Despite the above-mentioned shortcomings, the overall comparison between total displacements developed in the liquefiable layer is favourable (**Fig. 18**). The amplitude and the geometry of the displacement field is well predicted. The tendency for reduced displacements below the center of the foundation is predicted by the numerical analysis, but to a lesser extent than in the centrifuge experiment: a shortcoming linked to the predicted shear mechanism. Finally, the deeper displacement bulb at the left side of the foundation, which corresponds to accumulated rotation, is also predicted adequately well.

Artificially increased dissipation below the footing

In order to demonstrate the dominant role of the dissipation phenomena during shaking, and the importance of the over-prediction of pore pressures at the bottom of the soil column below the footing (P1), a second simulation is performed. The aim is to artificially force the pore pressures to dissipate in the area under the footing. To that end, the permeability is increased by an order of magnitude within the soil column below the footing. By no means is this proposed as a valid option for the realistic simulation of the developing failure mechanism. It is only an exploratory analysis, aiming to confirm the link

made to dissipation phenomena for the aforementioned interpretation of the failure mechanism.

Fig. 19 compares the simulated pore pressure time histories below the footing (P1 and P10) to the ones recorded in the centrifuge model test. As expected, the pore pressure build-up is decreased for both P1 and P10, with the differences being more pronounced at the deeper point (P1), where significant dissipation was observed in the centrifuge experiment. This drop in pore pressure build-up affects the response of the system and the developing failure mechanisms. **Fig. 20** illustrates the velocity vectors at $t = 14.64$ s, for the centrifuge experiment (**Fig. 20a**); and the two numerical analyses (**Fig. 20a,b**). The failure mechanism for the case of the increased permeability below the footing is more similar to the one observed in the centrifuge experiment. More precisely, the magnitude of velocity below the footing is lower and the observed failure mechanism is shallower (**Fig. 20c**). As shown in **Fig. 21a**, the accumulated shear strains at the end of the shaking are now more concentrated at the edges of the foundation. Furthermore, the simulated accumulated horizontal displacement u (**Fig. 21b**) are now closer to the ones observed in the centrifuge experiment (compare with **Fig. 16**). Overall, this simulation confirms the importance of appropriately modelling dissipation phenomena in order to capture displacement mechanisms below a foundation.

8. Conclusions

This paper studies the seismic response of a structure founded on a shallow foundation on liquefiable sand layer. A coupled hydromechanical analysis was conducted employing the FD code FLAC2d, modelling nonlinear soil response with PM4Sand. The model was calibrated using carefully executed element tests of Hostun (HN31) sand, conducted at ETH Zurich.

The calibrated model was then validated against a centrifuge model test that was previously conducted at the University of Cambridge (Adamidis & Madabhushi, 2018). The validation was performed following a strict procedure. The assessment was not restricted to the recorded acceleration, pore pressure, and settlement time histories, but also extended to the observed deformation mechanisms (extracted in the centrifuge test through image analysis).

Overall, the numerical simulation was shown to be in good agreement with the centrifuge experiment. The pore pressure build-up and the final foundation settlement and displacement fields were predicted fairly well. This is particularly encouraging given the strict calibration procedure that was followed, which was based on the void ratio of the sand in the centrifuge test. All model parameters were directly measured from the conducted classification and from element tests. None of the parameters was calibrated arbitrarily aiming to capture the centrifuge test results, which enhances our confidence on the process. The quality of the conducted element tests, on which the calibration was based, is considered of paramount importance in this respect.

Nevertheless, certain limitations of the numerical simulation were also observed. The limitation of the constitutive model in predicting the steep increase of pore water pressure during the first load cycle, is believed to have played a key role in the observed discrepancies in the prediction of settlement evolution. Although the accumulated co-seismic displacements were well reproduced, the failure mechanism, as observed in the centrifuge test, was not accurately captured by the numerical analysis. This discrepancy is attributed the numerical modelling of dissipation-related phenomena. In the numerical analysis, excess pore water pressures under the foundation failed to dissipate as fast as in the centrifuge experiment. This insight relating to the deformation mechanism could not have been revealed, if it wasn't for

the image analysis experimental results. To the best of our knowledge, this is the first time that such a comparison is conducted, enhancing the strictness of model validation.

Notation

h_{cm} :	<i>Height of the centre of mass</i>
h_{po} :	<i>Contraction rate parameter</i>
C_c :	<i>Coefficient of curvature</i>
C_u :	<i>Coefficient of uniformity</i>
D_{50} :	<i>Mean particle diameter</i>
D_r :	<i>Relative density</i>
G_{max} :	<i>Small-strain shear modulus</i>
G_o :	<i>Shear modulus coefficient</i>
G_s :	<i>Specific gravity</i>
K_o :	<i>Lateral earth pressure coefficient at rest</i>
K_w :	<i>Fluid bulk modulus</i>
e_{max} :	<i>Maximum void ratio</i>
e_{min} :	<i>Minimum void ratio</i>
r_u :	<i>Pore Water Pressure ratio</i>
ε_v :	<i>Volumetric Strain</i>
ρ_d :	<i>Dry mass density</i>
ρ_s :	<i>Wet mass density</i>
σ'_{vo} :	<i>Effective Vertical Stress</i>
φ_{cv} :	<i>Critical state friction angle</i>
CRR :	<i>Cyclic stress resistance</i>
B :	<i>B value</i>
G :	<i>Shear modulus</i>
N :	<i>Loading Cycles</i>
PP :	<i>Pore Pressure</i>
Q, R :	<i>Bolton's constants</i>
S :	<i>Ratio of the surface to the soil particles volume</i>
a :	<i>Acceleration</i>
e :	<i>Void ratio</i>
k :	<i>Permeability</i>
n :	<i>Porosity</i>
t :	<i>Time</i>
w :	<i>Settlement</i>
γ :	<i>Shear strain</i>
δ :	<i>Friction angle at the interface</i>
η :	<i>Viscosity</i>
θ :	<i>Rotation</i>

ν :	<i>Poisson ratio</i>
ξ :	<i>Damping ratio</i>
ρ :	<i>Unit weight</i>
τ :	<i>Shear Stress</i>

References

- Adamidis, O. Alber, S. Anastasopoulos, I. (2020). "Assessment of 3D-2020 printing of granular media for geotechnical applications". *Geotechnical Testing Journal*. Volume 43. Issue 3.
- Adamidis, O., and Madabhushi, S.P.G. 2016. Post-liquefaction reconsolidation of sand. *Proceedings of the Royal Society A: Mathematical, Physical and Engineering Science*, 472(2186): 20150745. doi:10.1098/rspa.2015.0745.
- Adamidis, O., and Madabhushi, S.P.G. 2018. Deformation mechanisms under shallow foundations on liquefiable layers of varying thickness. *Geotechnique*, 68(7): 1–13. doi:10.1680/jgeot.17.P.067.
- Arenson, L.U., and Springman, S.M. 2005. Triaxial constant stress and constant strain rate tests on ice-rich permafrost samples. *Canadian Geotechnical Journal*, 42(2): 412–430. doi:10.1139/t04-111.
- Arenson, L.U., Johansen, M.M., and Springman, S.M. 2004. Effects of volumetric ice content and strain rate on shear strength under triaxial conditions for frozen soil samples. *Permafrost and Periglacial Processes*, 15(3): 261–271. doi:10.1002/ppp.498.
- Arulanandan, K. and Scott, R.F., (1993) *Verification of Numerical Procedures for the Analysis of Soil Liquefaction Problems – Volume 1*, A.A. Balkema, Rotterdam, Netherlands.
- Arulnathan, R., Boulanger, R.W., and Riemer, M.F. 1998. Analysis of Bender Element Tests. *Geotechnical Testing Journal*, 21(2): 120–131. doi:10.1520/GTJ10750J.
- ASTM D4253-00. 2006. Standard Test Method for Minimum Index Density and Unit Weight of Soils Using a Vibratory Table. In *Annual book of ASTM standards*. doi:10.1520/D4253-16.
- ASTM D4254-00. 2006. ASTM D4254-00: Standard Test Methods for Minimum Index Density and Unit Weight of Soils and Calculation of Relative Density. *ASTM Standards*, I(Reapproved 2006): 9. doi:10.1520/D4254-00R06E01.1.3.

- Azeiteiro, R. N., Coelho, P.A.L.F., Taborda, D.M.G., and Grazina, J.C.D. 2017. Critical State–Based Interpretation of the Monotonic Behavior of Hostun Sand. *Journal of Geotechnical and Geoenvironmental Engineering*, 143(5): 04017004. doi:10.1061/(ASCE)GT.1943-5606.0001659.
- Bartelt, P., and von Moos, M. 2000. Triaxial test to determine a microstructure-based snow viscosity law. *Annals of Glaciology*, 31: 457–460. doi:10.3189/172756400781819761.
- Blewett, J., Blewett, I.J., and Woodward, P.K. 2000. Phase and amplitude responses associated with the measurement of shear-wave velocity in sand by bender elements. *Canadian Geotechnical Journal*, 37(2): 1348–1357. doi:10.1139/t01-107.
- Bolton, M.D. 1986. The strength and dilatancy of sands. *Géotechnique*, 36(I): 65–78.
- Boulanger, R.W., and Ziotopoulou, K. 2013. Formulation of a sand plasticity plane-strain model for earthquake engineering applications. *Soil Dynamics and Earthquake Engineering*, 53: 254–267. Elsevier. doi:10.1016/j.soildyn.2013.07.006.
- Boulanger, R.W., and Ziotopoulou, K. 2017. A sand plasticity model for earthquake engineering applications. *UCD/CGM-15(May)*: 1–114. doi:10.1016/j.soildyn.2013.07.006.
- Bray, J.D., and Macedo, J. 2017. 6th Ishihara lecture: Simplified procedure for estimating liquefaction-induced building settlement. *Soil Dynamics and Earthquake Engineering*, 102(August): 215–231. doi:10.1016/j.soildyn.2017.08.026.
- Bullock, Z., Karimi, Z., Dashti, S., Porter, K., Liel, A.B., and Franke, K.W. 2019. A physics-informed semi-empirical probabilistic model for the settlement of shallow-founded structures on liquefiable ground. *Géotechnique*, 69(5): 406–419. doi:10.1680/jgeot.17.p.174.
- Carrier, D.W. 2003. Goodbye, Hazen; Hello, Kozeny-Carman. *JOURNAL OF GEOTECHNICAL AND GEOENVIRONMENTAL ENGINEERING*, 129(November): 1054–1056.
- Cubrinovski, M., Bradley, B., Wotherspoon, L., Green, R., Bray, J., Wood, C., Pender, M., Allen, J., Bradshaw, A., Rix, G., Taylor, M., Robinson, K., Henderson, D., Giorgini, S., Ma, K., Winkley, A., Zupan, J., Rourke, T.O., Depascale, G., and Wells, D. 2011. *GEOTECHNICAL ASPECTS OF THE 22 FEBRUARY 2011 CHRISTCHURCH EARTHQUAKE*. 44(4): 205–226.

- Dafalias, Y.F., and Manzari, M.T. 2004. Simple Plasticity Sand Model Accounting for Fabric Change Effects. *Journal of Engineering Mechanics*, 130(6): 622–634.
- Dyvik, R., Berre, T., Lacasse, S., and Raadim, B. 1987. Comparison of truly undrained and constant volume direct simple shear tests. *Geotechnique*, 37(1): 3–10.
- Finn W. D. L. (1988) Dynamic analyses in geotechnical engineering. In: Von Thun JL, editor. *Earthquake engineering and soil dynamics II – recent advances in ground-motion evaluation*. Geotechnical Special Publication 20, ASCE; p. 523–91.
- Finn, W.D.L., and Vaid, Y.P. 1977. Liquefaction potential from drained constant volume cyclic simple shear tests. In *Proceedings of the sixth world conference on Earthquake Engineering*. p. Vol III, 2157-2162.
- Flavigny, E., Desrues, J., and Palayer, B. 1990. “Le sable d’Hostun «RF».” 53(67–69): 2–5. *Revue Française de Géotechnique*.
- Geonor (1968), "Description and Instruction for Use of Direct Simple-Shear Apparatus Model h-12", Geonor A/S, Oslo.
- Green, R. A, Ebeling, R. M. (2003) ‘Modeling the Dynamic Response of Cantilever Earth-Retaining Walls Using FLAC’ In: *Proceedings of the 3rd International Symposium on FLAC and FLAC3D Numerical Modeling in Geomechanics* (R. Brummer, P. Andrieux, C. Detournay, and R. Hart, eds.), A.A. Balkema Publishers, 2003 pp. 333–42.
- Ishibashi, I., and Zhang, X. 1993. UNIFIED DYNAMICS SHEAR MODULI AND DAMPING RATIOS OF SAND AND CLAY. *Soils and Foundations*, 33(1): 182–191. doi:10.1248/cpb.37.3229.
- Itasca. (2016) *FLAC – Fast Lagrangian Analysis of Continua*, Version 8.0, Itasca Consulting Group, Inc., Minneapolis, Minnesota.
- Khoury, N. Q. (1984): *Dynamic properties of soils*, Master Thesis, Department of civil Engineering, Syracuse University.
- Lambe, T.W. 1973. Predictions in soil engineering. *Geotechnique*, 23(2): 151–202. doi:10.1680/geot.1973.23.2.151.
- Lee, J.-S., and Santamarina, J.C. 2005. Bender Elements: Performance and Signal Interpretation. *Journal of Geotechnical and Geoenvironmental Engineering*, 131(9): 1063–1070. doi:10.1061/(ASCE)1090-0241(2005)131:9(1063).

- Okay, U.S., Dias, D., Thorel, L., and Rault, G. 2014. Centrifuge modeling of a pile-supported granular earth-platform. *Journal of Geotechnical and Geoenvironmental Engineering*, 140(2). doi:10.1061/(ASCE)GT.1943-5606.0001004.
- Parker Hannifin Corporation (2013). Duxseal Sealing and caulking compound. Technical report.
- Pickering, D.J. 1969. A simple shear machine for soil. THE UNIVERSITY OF BRITISH COLUMBIA.
- Popescu, R., and Prevost, J.H. 1993. Centrifuge validation of a numerical model for dynamic soil liquefaction. *Soil Dynamics and Earthquake Engineering*, 12(2): 73–90. doi:10.1016/0267-7261(93)90047-U.
- Sassa, S., and Takagawa, T. 2019. Liquefied gravity flow-induced tsunami: first evidence and comparison from the 2018 Indonesia Sulawesi earthquake and tsunami disasters. *Landslides*, 16(1): 195–200. *Landslides*. doi:10.1007/s10346-018-1114-x.
- Shirley, D.J. 1978. An improved shear wave transducer. *The Journal of the Acoustical Society of America*, 63(Issue 5): 1643–1645. doi:https://doi.org/10.1121/1.381866.
- Shirley, D.J., and Hampton, L.D. 1978. Shear-wave measurements in laboratory sediments. *The Journal of the Acoustical Society of America*, 63(2): 607–613. doi:10.1121/1.381760.
- Skempton, A.W. 1954. The pore-pressure coefficients a and b . *Geotechnique*, 4(4): 143–147. doi:10.1680/geot.1954.4.4.143.
- Steedman, R. S. and Madhabushi, S. P. G. (1991). Wave propagation in sand medium. In *The 4th International Conference on Seismic Zonation*. EERI
- Tasiopoulou, P., and Chaloulos, Y. 2019. 3D and 2D simulations of liquefaction-induced settlements of shallow foundations using Ta-Ger model. pp. 5241–5248.
- Viggiani, G., and Atkinson, J.H. 1995. Interpretation of bender element tests. *Geotechnique*, 45(1): 149–154. doi:10.1680/geot.1995.45.1.149.
- White, D.J., Take, W.A., and Bolton, M.D. 2003. Soil deformation measurement using particle image velocimetry (PIV) and photogrammetry. *Geotechnique*, 53(7): 619–631. doi:10.1680/geot.2003.53.7.619.
- Wu, J., Kammerer, A.M., Riemer, M.F., Seed, R.B., and Pestana, J.M. 2004. LABORATORY STUDY OF LIQUEFACTION TRIGGERING CRITERIA. In *13 th World Conference on Earthquake Engineering*. pp. 74–76. doi:10.1016/0093-6413(82)90023-4.

- Yasuda, S., Harada, K., Ishikawa, K., and Kanemaru, Y. 2013. Characteristics of liquefaction in Tokyo Bay area by the 2011 Great East Japan Earthquake. *Soils and Foundations*, 52(5): 793–810. Elsevier. doi:10.1016/j.sandf.2012.11.004.
- Ziotopoulou, K. 2018. Seismic response of liquefiable sloping ground: Class A and C numerical predictions of centrifuge model responses. *Soil Dynamics and Earthquake Engineering*, 113(January): 744–757. Elsevier Ltd. doi:10.1016/j.soildyn.2017.01.038.
- Ziotopoulou, K., and Boulanger, R.W. 2013a. NUMERICAL MODELING ISSUES IN PREDICTING POST-LIQUEFACTION RECONSOLIDATION. (March 2012).
- Ziotopoulou, K., and Boulanger, R.W. 2013b. Numerical Modeling Issues in Predicting Post-Liquefaction Reconsolidation Strains and Settlements. 10th International Conference on Urban Earthquake Engineering (10CUEE), (1992): 469–475.
- Ziotopoulou, K., and Boulanger, R.W. 2016. Plasticity modeling of liquefaction effects under sloping ground and irregular cyclic loading conditions. *Soil Dynamics and Earthquake Engineering*, 84: 269–283. Elsevier. doi:10.1016/j.soildyn.2016.02.013.

Table 1. Constant volume direct simple shear test results.

e (–)	σ'_{vo} (kPa)	CSR (–)	Load cycles (–)	
			$r_u = 0.98\%$	$\gamma = 3.75\%$
0.932	100	0.049	378.9	379.6
0.913	100	0.079	14.0	14.6
0.910	100	0.097	4.0	3.7
0.906	100	0.118	3.0	2.7
0.829	100	0.177	3.5	3.6
0.818	100	0.146	8.9	10.0
0.836	100	0.119	15.4	15.7
0.843	100	0.098	87.0	88.7
0.711	100	0.265	4.0	4.2
0.730	100	0.247	3.5	4.7
0.719	100	0.179	17.2	20.1
0.708	100	0.127	129.0	153.3

Table 2. Calibrated Hostun (HN31) sand parameters for OA6 experiment.

Parameter	Meaning	Source	Value
e (-)	Void ratio	measured	0.788
n (-)	Porosity	$e/(1+e)$	0.441
G_s (Mg/m ³)	Specific gravity	measured	2.65
ρ_d (Mg/m ³)	Dry mass density	$e/(1+G_s)$	1.48
ρ_s (Mg/m ³)	Wet mass density	$\rho_d \times (1+e/G_s)$	1.92
k (m/s)	Permeability	$2.92 \times 10^{-3} \times e^3/(1+e)$	7.98E-04

Table 3. Calibrated PM4sand parameters for OA6 experiment.

Parameter	Meaning	Source	Value
e_{min} (-)	Minimum void ratio	<i>measured from e_{min} test</i>	0.648
e_{max} (-)	Maximum void ratio	<i>measured from e_{max} test</i>	1.049
D_r (%)	Relative density	$(e_{max}-e)/(e_{max}-e_{min})$	0.65
G_o (-)	Shear modulus coefficient	$293 \times e^2/(1+e)$	780.21
h_{p0} (-)	Contraction rate parameter	<i>fitting targeting CRR curves</i>	0.04
ϕ_{cv} (°)	Critical state friction angle	<i>measured from drained triaxial tests</i>	33.8
K_o (-)	Lateral earth pressure coefficient at rest	$1-\sin(\phi_{cv})$	0.444
ν (-)	Poisson ratio	$K_o/(1+K_o)$	0.307
Q (-)	Bolton's constant	<i>measured from drained triaxial tests</i>	8.4
R (-)	Bolton's constant	<i>measured from drained triaxial tests</i>	0.78

Figure captions

Fig. 1. Triaxial Bender element tests: (a) sample preparation; and (b) experimental setup.

Fig. 2. Example of input and output signals. The points correspond to: (A) first deflection, (B) first maximum, (C) zero after first bump, (D) first major peak and (P) peak of input.

Fig. 3. Estimation of small-strain shear modulus (G_{max}) in function of mean effective stress p' using the zero after the first bump method.

Fig. 4. Comparison of measured small-strain shear modulus (in normalized form) to the expression proposed by Azeiteiro et al. (2017).

Fig. 5. Simple shear testing: (a) modified Geonor direct simple shear apparatus; (b) wire reinforced membrane; (c) shear stress–shear strain ($\tau - \gamma$) during a drained direct simple shear test of a sample with initial $e = 0.829$ and $\sigma'_{vo} = 50$ kPa; and (d) volumetric strain–shear strain ($\varepsilon_v - \gamma$) response.

Fig. 6. Comparison of DSS test results with the analytical expression of Ishibashi & Zhang (1993) for 3 levels of vertical effective stress (σ'_v): (a) $G - \gamma$ degradation curves; and (b) $\xi - \gamma$ curves. Comparison of FLAC simulations with Ishibashi & Zhang (1993) for the same three stress levels: (c) $G - \gamma$ degradation; and (d) $\xi - \gamma$.

Fig. 7. Typical constant volume simple shear test (CVSST) results (left column) compared to simulation results (right column) for a sample of $e = 0.836$ and initial vertical effective stress $\sigma'_{vo} = 100$: (a) Shear stiffness degradation; (b) stress path; and (c) effective vertical stress (σ'_v) versus loading cycles (N).

Fig. 8. Cyclic resistance ratio (CRR) as a function of load cycles (N) for liquefaction triggering (considering the two criteria $r_u = 0.98$ and $\gamma = 3.75$ % in SA) and void ratio (e). The DSS test results are represented by dots, and the lines correspond to the prediction of the fitted analytical expression (Eq. 3) for the DSS tests and of the simulated centrifuge test ($e = 0.788$).

Fig. 9. Model calibration: CRR in function of load cycles (N) for $\sigma'_{vo} = 100$ kPa and $e = 0.788$: Comparison of experimental results (black line) to numerical simulation results with PM4Sand calibrated according to: (a) 3 different liquefaction triggering criteria ($\gamma = 3.75$ %, $r_u = 0.98$, and average) and $h_{po} = 0.04$; (b) average criterion, varying h_{po} ; (c) $r_u = 0.98$ criterion and $h_{po} = 0.04$, varying the shear modulus coefficient G_o ; and (d) $\gamma = 3.75$ % criterion and $h_{po} = 0.04$, varying the shear modulus G_o .

Fig. 10. Cross-section of OA6 centrifuge model test (top) along with the seismic excitation (bottom), as measured by accelerometer A5 (both in prototype scale).

Fig. 11. Outline of the numerical model.

Fig. 12. Comparison of computed pore pressures (PP) with those measured in the centrifuge experiment: (a) in the free field; and (b) below the structure

Fig. 13. Comparison of computed accelerations with those measured in the centrifuge model test.

Fig. 14. Comparison between computed settlement–rotation (w – θ) response with that measured in the centrifuge model test.

Fig. 15. Comparison between numerical analysis and centrifuge experiment: accumulated shear strain contours at the end of the shaking.

Fig. 16. Comparison between numerical analysis and centrifuge experiment: accumulated horizontal displacement contours at the end of the shaking.

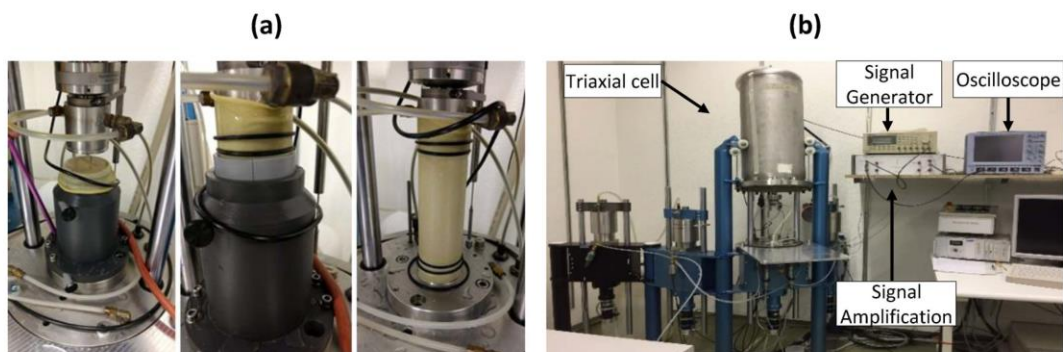
Fig. 17. Comparison between numerical analysis and centrifuge experiment: accumulated vertical displacement contours at the end of the seismic excitation.

Fig. 18. Comparison between numerical analysis and centrifuge experiment: accumulated total displacement contours at the end of the seismic excitation.

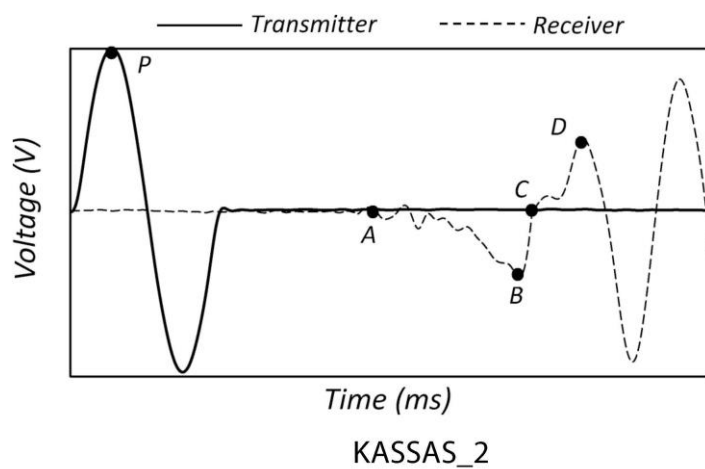
Fig. 19. Simulation assuming increased permeability: comparison of computed pore pressures (PP) below the structure with those measured in the centrifuge model test.

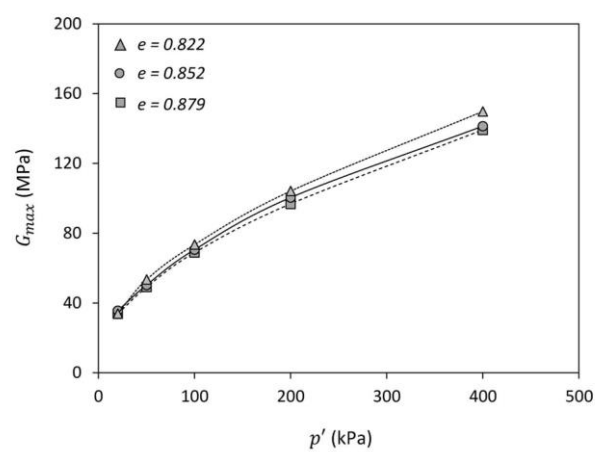
Fig. 20. Velocity vectors at $t = 14.64$ s for: (a) centrifuge experiment; (b) numerical simulation; and (c) numerical simulation with increased permeability.

Fig. 21. Simulation assuming increased permeability: (a) accumulated shear strain; and (b) horizontal displacement contours at the end of the seismic excitation.

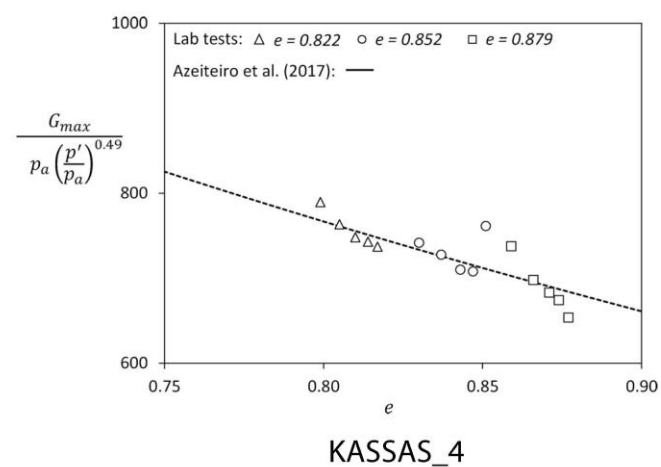


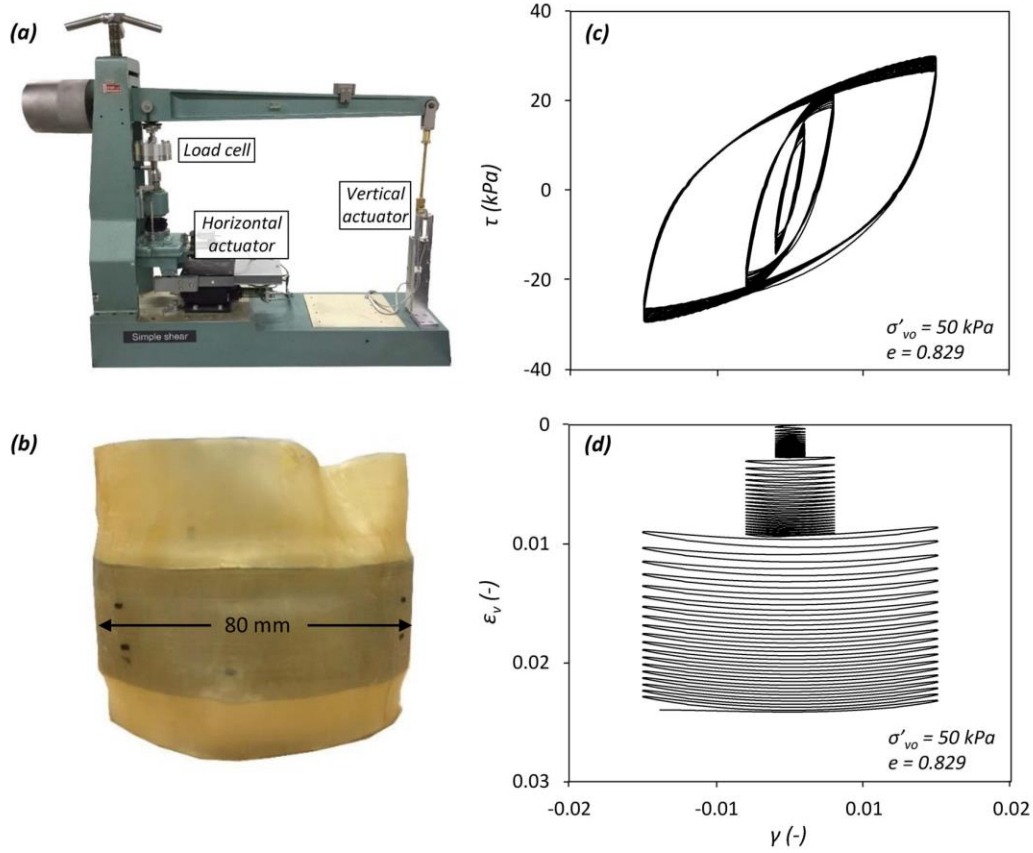
KASSAS_1



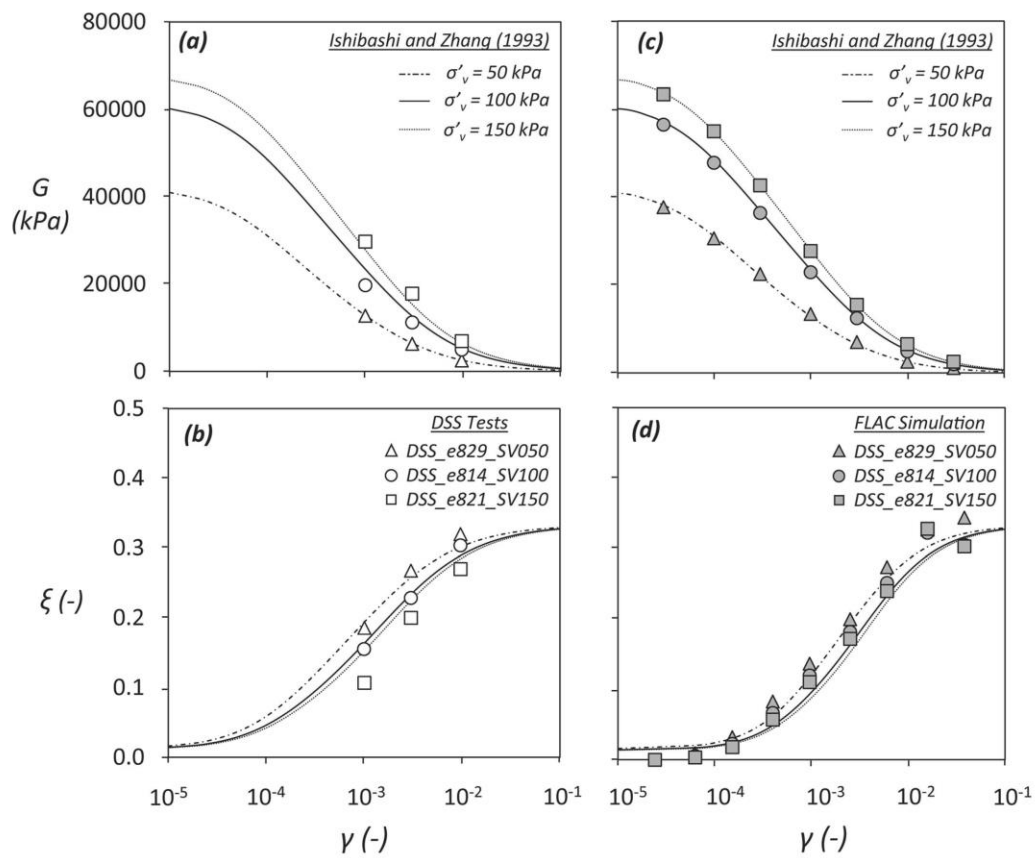


KASSAS_3

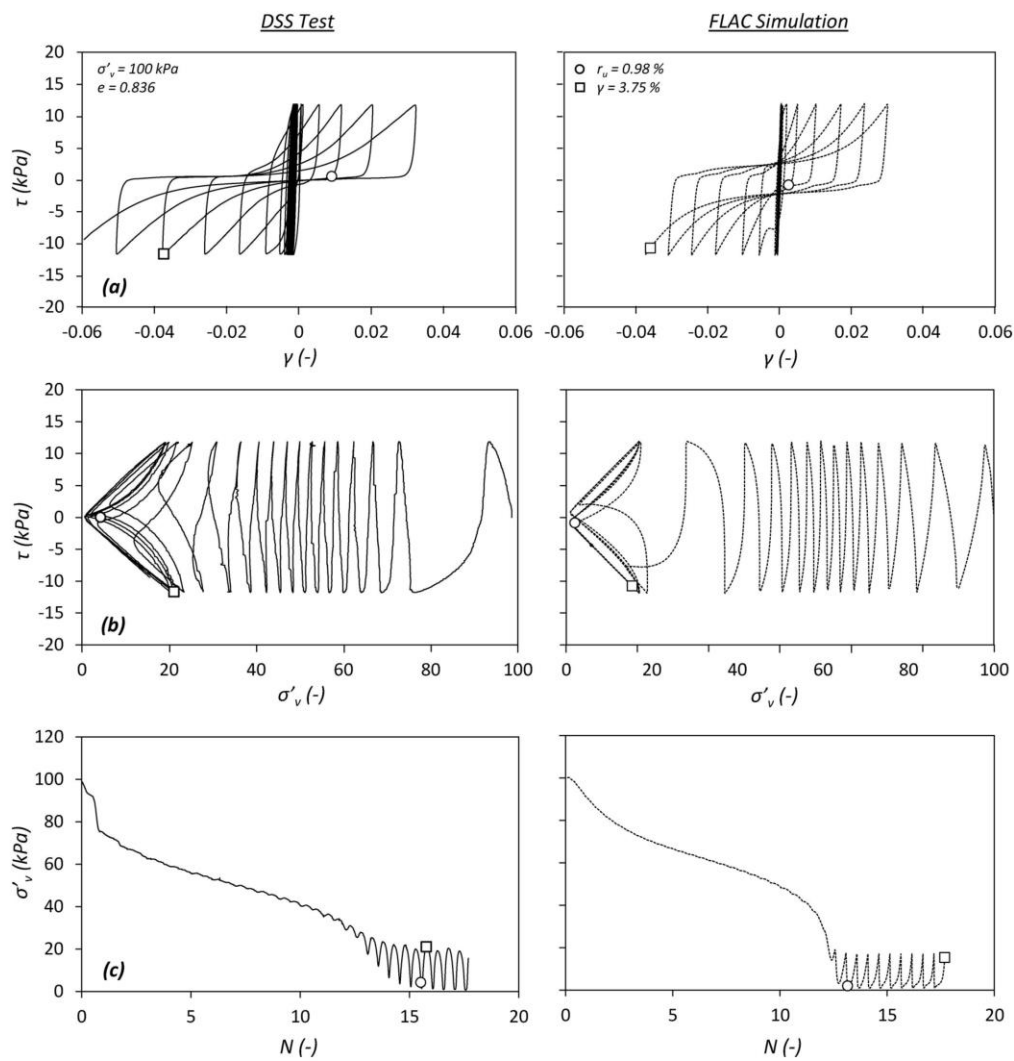




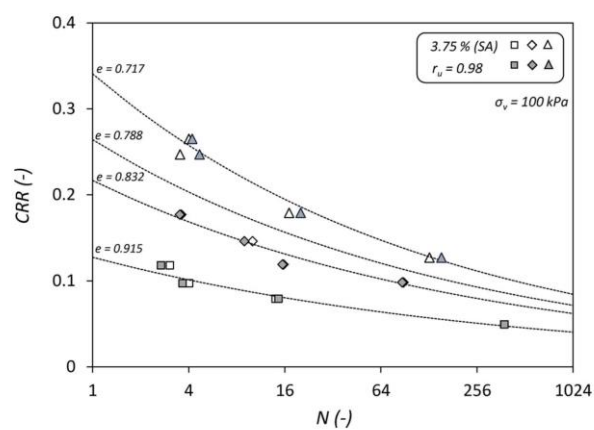
KASSAS_5



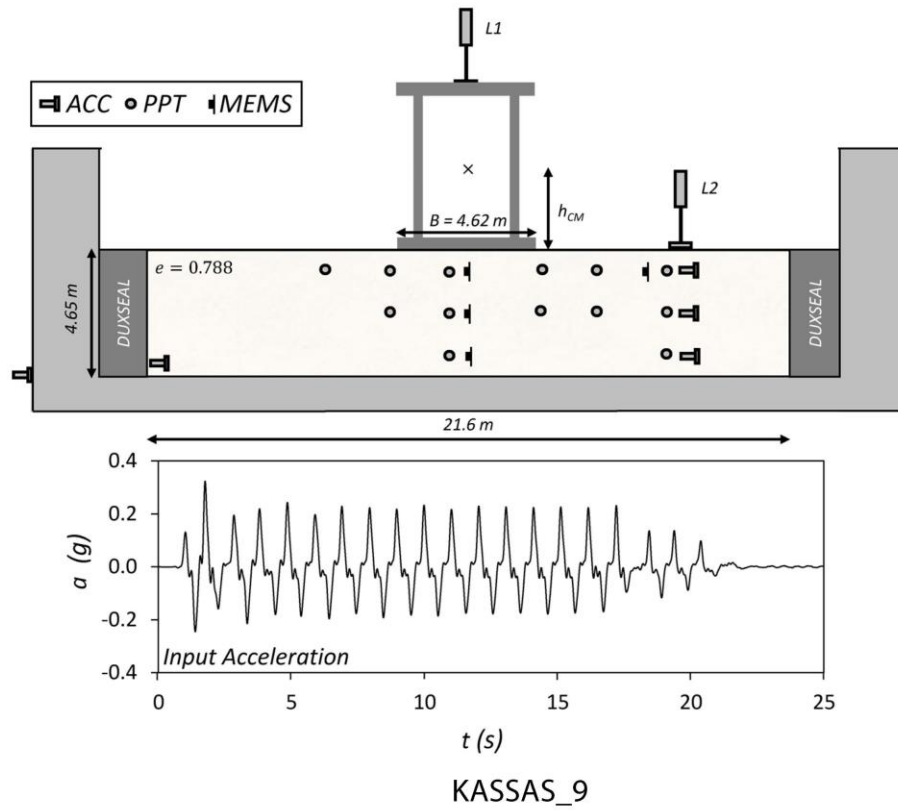
KASSAS_6

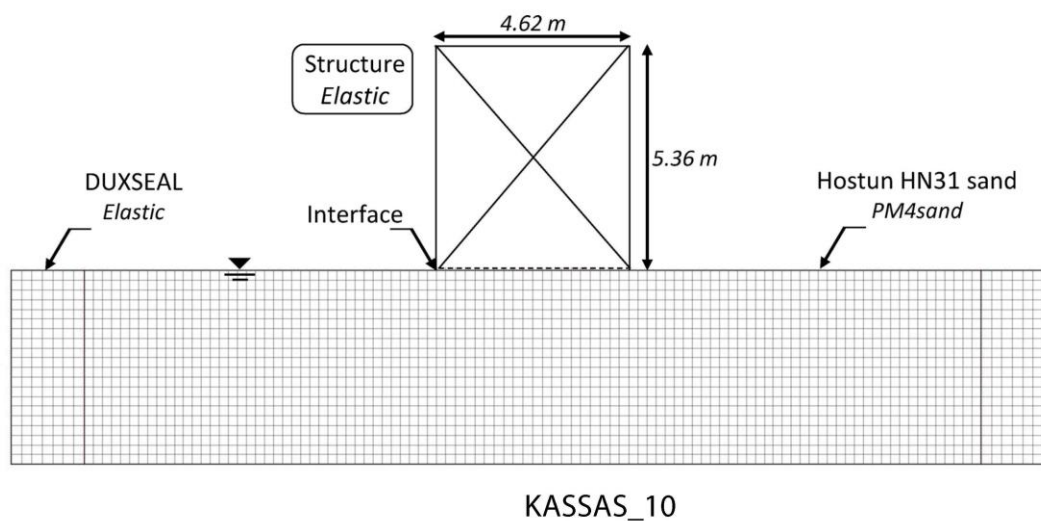


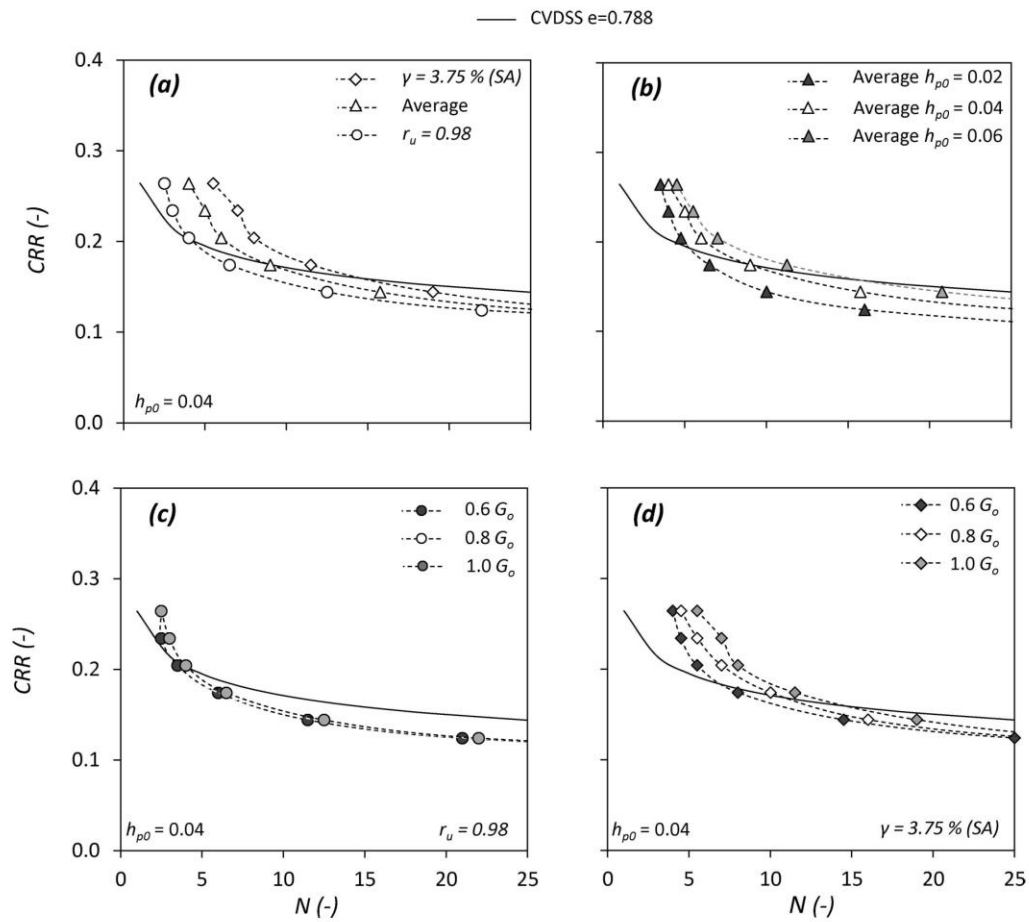
KASSAS_7



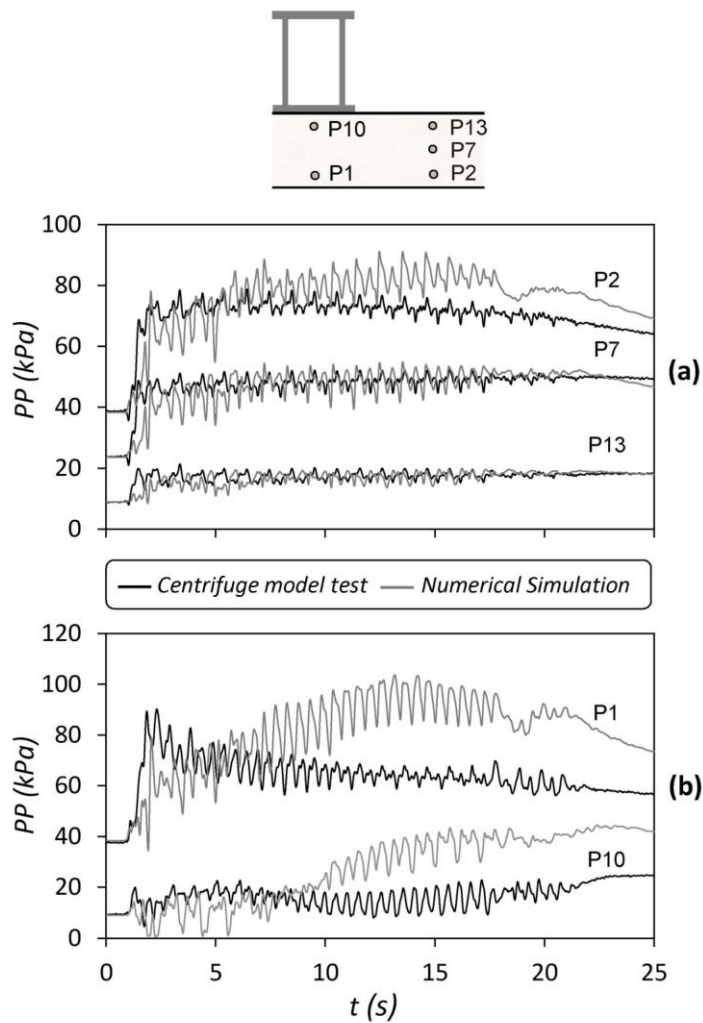
KASSAS_8



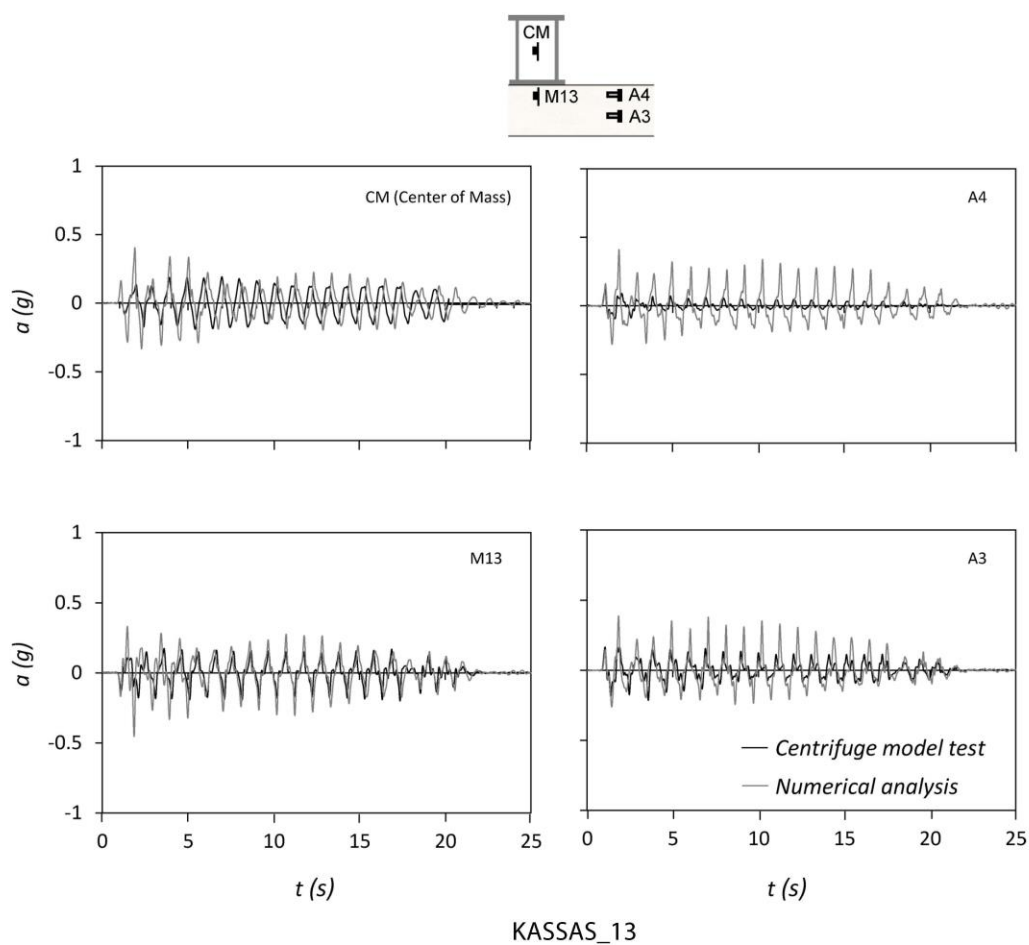


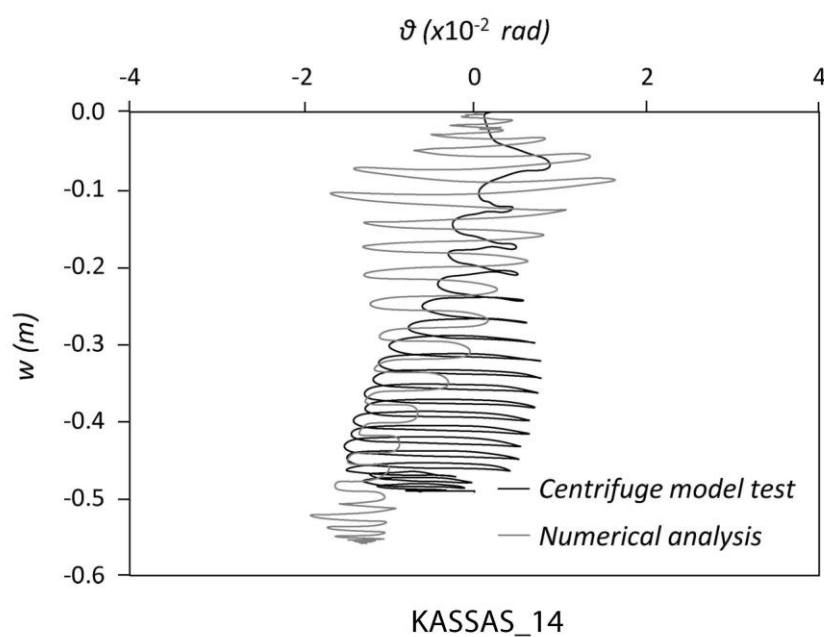


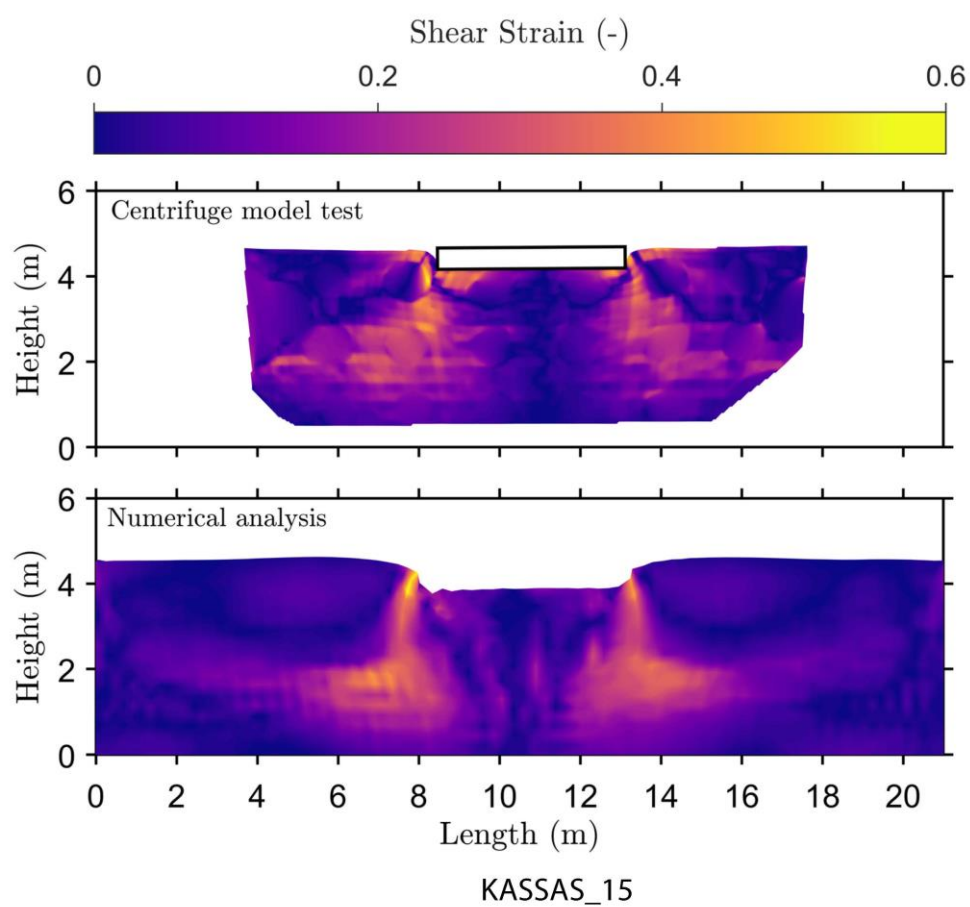
KASSAS_11

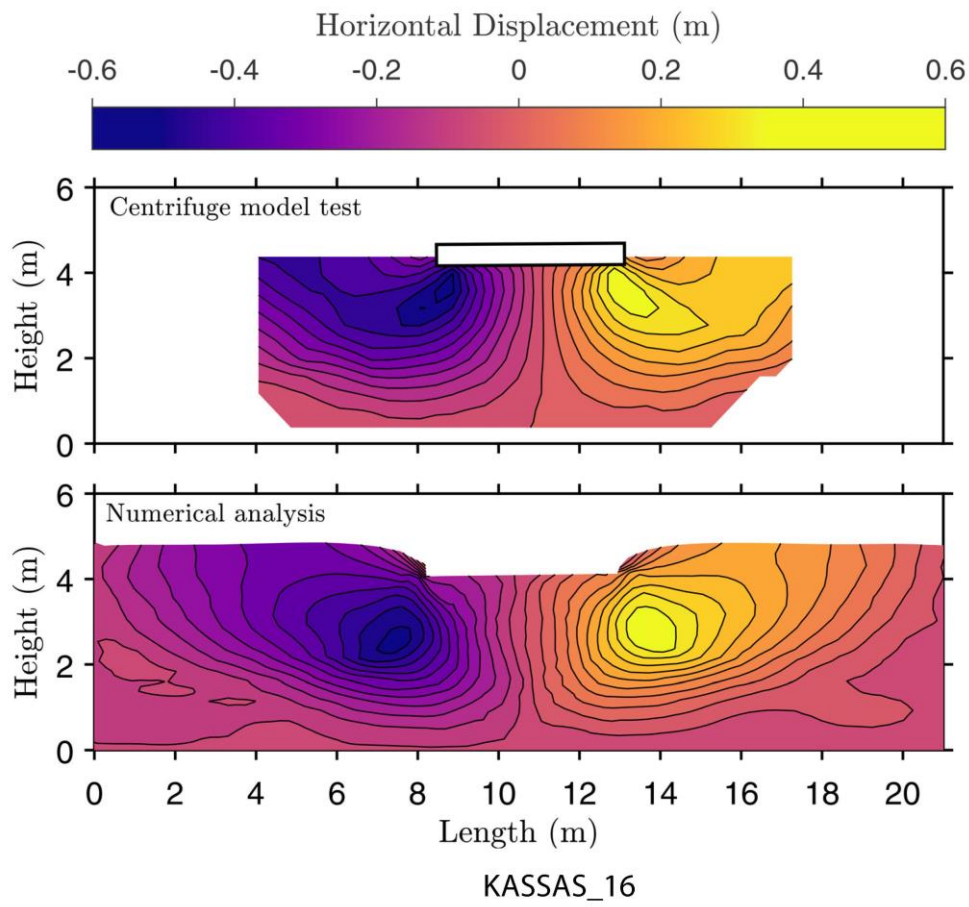


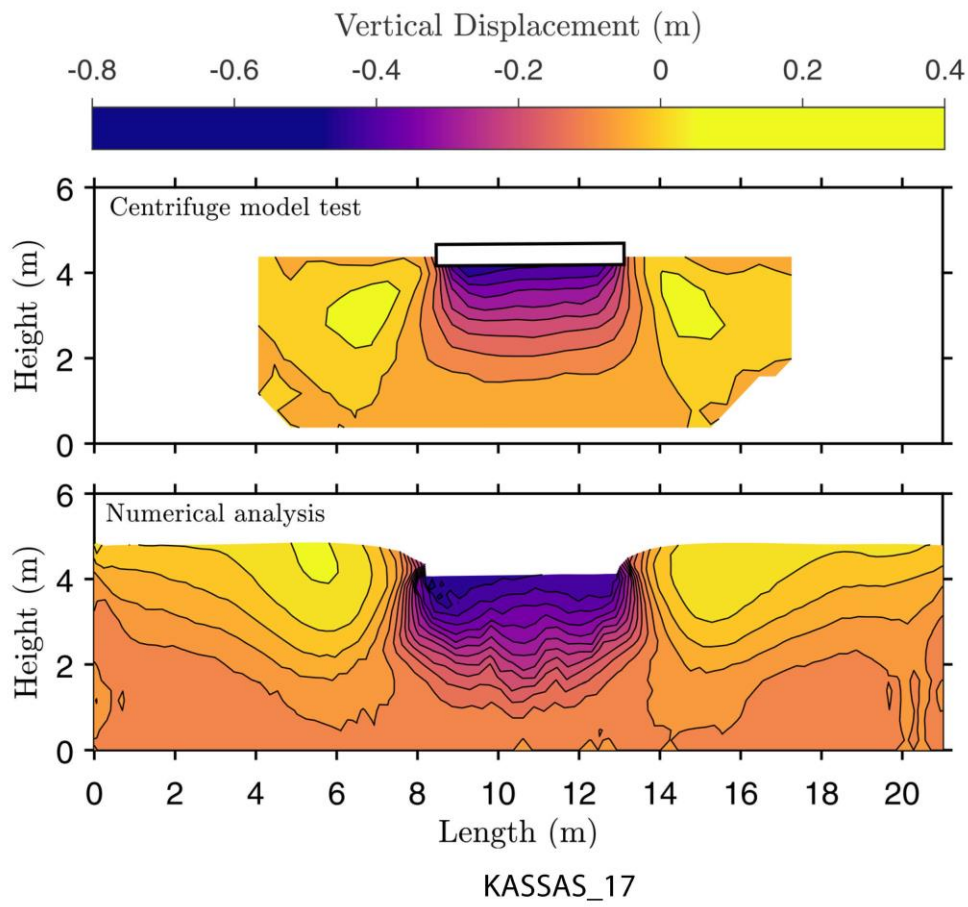
KASSAS_12

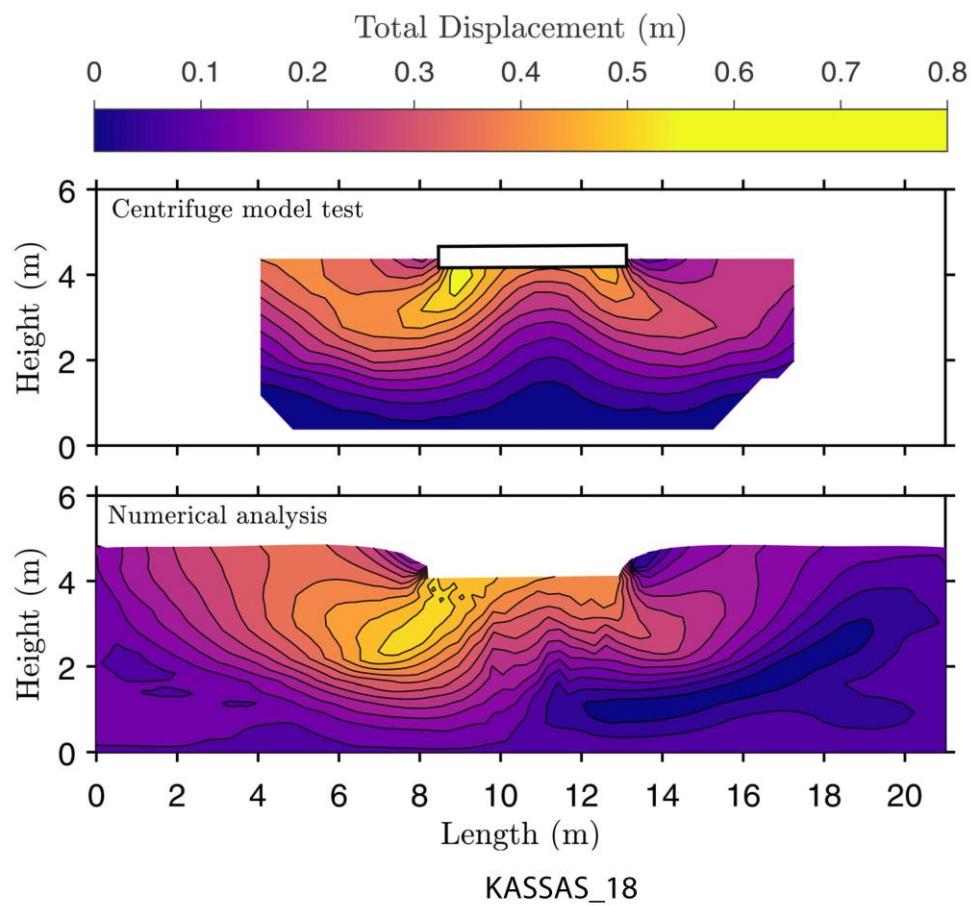


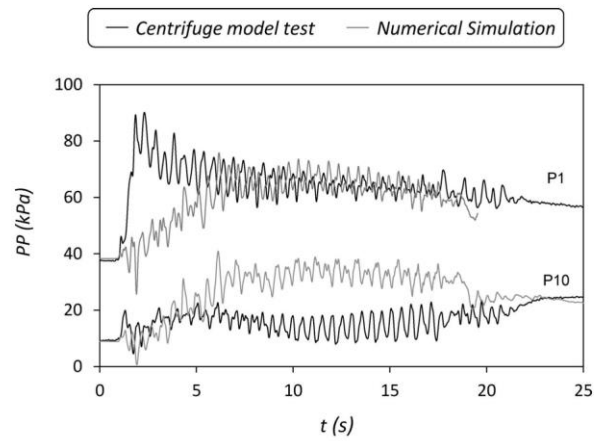




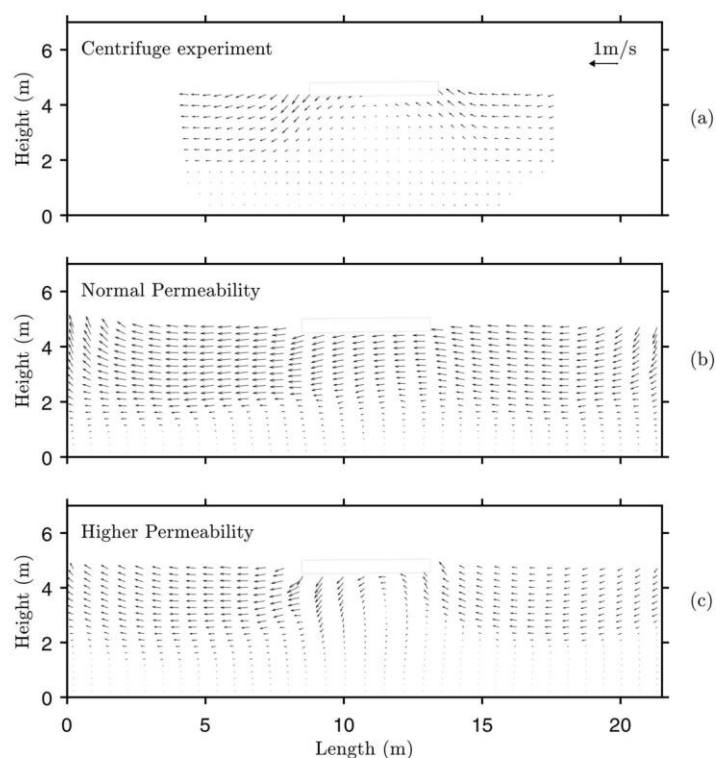








KASSAS_19



KASSAS_20

